Oceanic influence and lapse rate changes dominate the recent amplified Saharan warming

Li Zhuo[1], Brian E. J. Rose[1]

[1]Department of Atmospheric and Environmental Sciences, University at Albany, State University of New York, Albany, NY, USA

Key Points:

- The observed Saharan warming since 1979 is largely a result of the SST change rather than direct anthropogenic GHG radiative forcing.
- The dominant factor driving Saharan warming is the anomalous atmospheric energy transport from the warming ocean.
- Lapse rate and water vapor feedbacks both amplify Saharan warming relative to the average tropical land in response to the SST forcing.

Zhuo, L., & Rose, B. E. J. (2024). Oceanic influence and lapse rate changes dominate the recent amplified Saharan warming. Geophysical Research Letters, 51, e2023GL106961. https://doi.org/10.1029/2023GL106961

Received 23 OCT 2023
Accepted 23 DEC 2023
Published 12 January 2024

Corresponding author: Li Zhuo, lzhuo@albany.edu

Abstract

The surface air temperature (SAT) over the Sahara Desert has increased at a much faster rate than average tropical land in recent decades. This study examines the relative roles of anthropogenic greenhouse gas (GHG) forcing and sea surface temperature (SST) change in the observed Saharan temperature increase during boreal warm season from 1979 to 2020 using atmospheric general circulation model simulations. It is found that the SST forcing dominates the observed Saharan warming. Further analysis shows that the warming ocean forces the Saharan SAT increase by moving more energy to the Sahara Desert, while the water vapor feedback plays a secondary role. The reason for the stronger Saharan warming than the average tropical land given the same SST forcing is also explored. We found that the largest contributor to the warming contrast is the lapse-rate feedback, which is attributable to the difference in the vertical warming profile.

Plain Language Summary

Sahara Desert has experienced a stronger warming than the tropical land on average since 1979. Debates continue on whether the amplified Saharan warming is a response to the remote SST change or the radiative forcing brought about by the increasing anthropogenic GHG. In this study, we quantify the relative contributions of these two forcing agents to the observed Saharan temperature increase. It is found that the observed Saharan warming is largely controlled by the remote SST forcing. As the ocean warms up, it acts to transport more energy to the Sahara Desert and warms the surface. The warming contrast between the Sahara Desert and the average tropical land is found to be dominated by the lapse-rate feedback, which favors the Saharan warming but suppresses the average tropical land warming. The difference in lapse-rate feedback is a result of the different vertical warming structure over the Sahara Desert and average tropical land.

1 Introduction

The increase of surface air temperature (SAT) over the Sahara Desert, one of the world's largest deserts, has been proceeding at a much faster rate than the average tropical land since 1979 (Cook & Vizy (2015); Lavaysse et al. (2016); Vizy & Cook (2017)), which is termed "Desert Amplification" (hereafter DA). The amplified Saharan warming is most pronounced during the boreal warm season (JJASON) and features a bottom-heavy vertical profile (Cook & Vizy (2015); Wei et al. (2017); Zhou (2021)).

Many studies have suggested that the amplified Saharan warming is a local response to the radiative forcing driven by escalating anthropogenic greenhouse gas (GHG) emissions (Cook & Vizy (2015); Liu et al. (2001); Liu et al. (2002); Zhou et al. (2015); Zhou et al. (2016)). For instance, through the analysis of a set of model outputs from the Coupled Model Intercomparison Project phase 5 (CMIP5) archive, Zhou et al. (2015) showed that the simulations with only natural forcings fail to reproduce the major features of the observed Saharan warming and DA. Similarly, in the future projection studies, the surface elevated radiative forcing resulting from the anthropogenic GHG is argued to be responsible for DA in the 21st century (Liu et al. (2001); Liu et al. (2002)).

A contrary view was advanced by Skinner et al. (2012), who showed that sea surface temperature (SST) change plays a dominant role in shaping the temperature increase over the Sahara Desert in the 21st century, while the influence of the change in GHG is negligible. The result from Skinner et al. (2012) highlights the dominance of SST forcing in determining the Saharan warming, which is consistent with previous work on land sea warming contrast (Andrews et al. (2009); Byrne & O'Gorman (2013); Byrne & O'Gorman (2018); Compo & Sardeshmukh (2009); Dommenget (2009); Lambert & Chiang (2007)). However, Skinner et al. (2012) did not examine the mechanism driving the SST-induced Saharan temperature response. The key role of SST forcing is also evidenced in studies highlighting the strong water vapor feedback over the Sahara Desert (Evan et al. (2015); Zhou et al. (2016); Zhuo

& Zhou (2022)), as most of the increased moisture over the land originates from the ocean (Trenberth et al. (2007)).

According to Compo & Sardeshmukh (2009), the oceanic warming forces the land temperature increase by moving extra energy from the ocean to the land. The key role of heat transport anomaly between land and ocean in maintaining a constant land sea warming ratio has also been reported by Lambert et al. (2011) and Toda et al. (2021). Without the anthropogenic GHG forcing, it is expected that the heat transport anomaly acts as the external forcing and increases the surface temperature over the Sahara Desert (Lambert et al. (2011)). However, the SST-induced Saharan temperature increase is also subject to local climate feedbacks, such as the water vapor and lapse-rate feedbacks (Colman & Soden (2021)). The relative contributions of heat transport anomaly and climate feedbacks to the observed Saharan temperature increase is still unclear.

In this study, we make use of an atmospheric general circulation model (AGCM) to quantify the relative contributions of anthropogenic GHG radiative forcing and remote SST forcing to the observed amplified Saharan warming in the boreal warm season since 1979. Note that the SST forcing defined in our study denotes the net effects of the observed SST change over the globe (Deser & Phillips (2009); Folland et al. (1998)). 1979 is chosen as the beginning year for consistency with previous studies (Cook & Vizy (2015); Zhou et al. (2015)) and availability of the satellite-derived SST (Deser et al. (2010)). As will be shown later, SST forcing yields a much larger contribution to the recent observed Saharan temperature increase than the direct anthropogenic GHG radiative forcing. To explore the process whereby the SST forcing induces the Saharan warming, we isolate the effects of the SST change in one experiment and perform a decomposition analysis of the observed Saharan temperature increase, similar to previous studies on Arctic Amplification (Pithan & Mauritsen (2014)). This decomposition allows us to assess the impacts of each physical process on the observed temperature increase over the Sahara Desert, and the stronger Saharan warming than the average tropical land given the same oceanic forcing. We focus on the warming contrast between the Sahara Desert (20°N-30°N; 10°W-30°E) and the average tropical land (30°S-30°N) as SST is prescribed in our simulations.

2 Model simulations and datasets

We utilize the NCAR Community Atmosphere Model version 4 (CAM4) in this study. CAM4 is the atmospheric component of the Community Earth System Model (CESM) (Hurrell et al. (2013)). CAM4 used here has 26 vertical levels and is run on a finite-volume grid with a horizontal resolution of approximately 1.9 latitude and 2.5 longitude (Gent et al. (2011)).

To isolate the SST effects from the anthropogenic GHG radiative forcing, here we force the CAM4 model with different forcing combinations, following previous studies (Deser & Phillips (2009); Folland et al. (1998); He & Soden (2015); Li et al. (2020); Shaw & Voigt (2015); Shen et al. (2020)). In the ALL experiment, the model is forced with the observed evolution of monthly SST, GHG and other forcings (ozone, solar variation, anthropogenic and natural aerosols). In the NOSST experiment, the atmospheric forcings are prescribed as in ALL but the SST is fixed to the annual cycle in 1979. In the NOGHG experiment, the model is forced with the same SST and other forcings as in ALL but with the GHG fixed to the annual cycle in 1979. Note that these two mechanism-denial experiments only enable the examination of the net effects of certain types of forcing, not their operating mechanism. In order to isolate and elucidate the mechanism associated with the SST forcing, here we conduct another process-oriented experiment in which only the year-to-year observed SST is prescribed while the atmospheric forcings are fixed to the annual cycle in 1979 (SSTONLY). All of these simulations start from 1st January 1979 and end on 31st December 2020.

The SST and sea ice concentration dataset used in this study is described in Hurrell et al. (2008). The historical and Representative Concentration Pathway 8.5 (RCP8.5) atmospheric forcings are used before and after December 2005, respectively. We utilize the fifth major global reanalysis produced by European Centre for Medium-Range Weather Forecasts (ERA5; Hersbach et al. (2020)) as the benchmark for the Saharan temperature response in all simulations. The radiative kernel dataset by Pendergrass et al. (2018) is employed in this study to perform the climate feedback and temperature decomposition analysis.

3 Saharan warming and DA in model simulations

The interannual variability and linear trends of the Saharan and average tropical land SAT in the boreal warm season are shown in Figure 1. We calculate the trends via ordinary least-squares regression and the uncertainty bounds denote the 95 % confidence interval. In ERA5, the Saharan temperature features a rapid increase at a rate of 0.43±0.08 K per decade, which is close to the corresponding trend in ALL (0.47±0.11 K per decade) (Figure 1b). The Pearson correlation coefficient between ERA5 and ALL is 0.77 (calculated without smoothing) and statistically significant at the 99 % level of confidence (Figure 1a). The spatial warming pattern over the Sahara Desert in ALL also bears close resemblance with that in ERA5 (Figures 2a, b). Comparison between ERA5 and ALL indicates that ALL has reliably reproduced the surface warming over the Sahara Desert to a large extent (Figure 1 and Figures 2a-b).

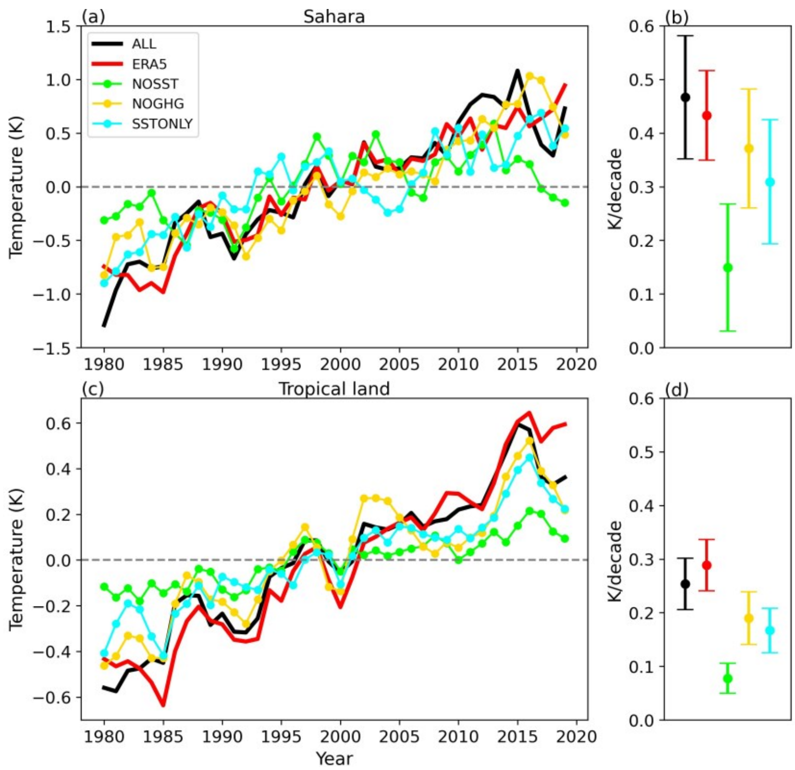

Figure 1. (a) Interannual variability of the SAT anomalies (K) over the Sahara Desert in the boreal warm season from ALL (black), ERA5 (red), NOSST (green), NOGHG (gold) and SSTONLY (cyan). All time series are smoothed with a 3-year running average. (b) corresponding linear trends (K/decade) of the SAT in (a). Error bars denote the 95 % confidence intervals. (c) and (d): same as (a) and (b) but for the average tropical land (30°S-30°N).

In NOSST with the SST forcing turned off, the Saharan warming trend is reduced to 0.15±0.12 K per decade (Figure 1b). In comparison, when the GHG forcing is deactivated, the trend of the Saharan temperature is about 0.37±0.11 K per decade, which still accounts for 79 % of ALL (Figure 1b). Comparison between NOSST and NOGHG highlights the dominant role of SST forcing in the observed Saharan temperature increase. The discrepancy in the spatial warming pattern between different experiments also supports that the SST forcing makes a much larger contribution to the Saharan temperature increase than the anthropogenic GHG forcing (Figures 2a-d). Without the SST forcing, the Saharan warming is strongly dampened and a large portion of the temperature trend is statistically insignificant (Figure 2c), consistent with Skinner et al. (2012). Note that the sum of the trend in SSTONLY (0.31 K per decade) and NOSST (0.15 K per decade) is close to that in ALL (0.47 K per decade) (Figure 1b), indicating the Saharan temperature response to the SST forcing and atmospheric radiative forcing are approximately linear and additive, which is in agreement with previous studies (Deser & Phillips (2009); Shen et al. (2020); Skinner et al. (2012)).

In comparison to the Sahara Desert, the average tropical land warms at a slower rate in ERA5 (0.29±0.05 K per decade) and ALL (0.25±0.05 K per decade) (Figure 1d). The average tropical land warming are weakened in both NOGHG and NOSST compared to ALL. However, the warming rate in NOSST (0.08±0.05 K per decade) is less than half that of NOGHG (0.19±0.05 K per decade) (Figure 1d), highlighting the dominant control of oceanic warming on the tropical land warming (Byrne & O'Gorman (2018); Byrne (2021)). DA is also evident in SSTONLY as the temperature trend over the Sahara Desert (0.31±0.12 K per decade) is about twice the average tropical land (0.17±0.04 K per decade) (Figures 1b, d).

4 Surface temperature change attribution

In this section, we will decompose the surface temperature change over the Sahara Desert and average tropical land in SSTONLY using a conventional surface temperature change attribution method (Goosse et al. (2018); Henry et al. (2021); Pithan & Mauritsen (2014); Stuecker et al. (2018)). By conducting such a decomposition, we aim to address these two questions: (i) how does the SST forcing force the Sahara Desert to warm up? (ii) With the same oceanic forcing, what drives the faster Saharan warming than the average tropical land?

We take the change as the difference of the variable averaged between the first (1979-1988) and last (2011-2020) decades of the simulation. One can decompose the SAT change $\triangle T_s$ over a specific area as follows (Goosse et al. (2018); Henry et al. (2021)):

$$\triangle T_s = \left(-\frac{1}{\overline{\lambda_0}}\right)(F + \triangle R_{PL} + \triangle R_{WV} + \triangle R_{LR} + \triangle R_{CD} + \triangle R_{AL} + Q_s + \triangle AET), \quad (1)$$

where $\overline{\lambda_0}$ is the global mean Planck feedback parameter ($W\,m^{-2}K^{-1}$), F is the radiative forcing, $\triangle R_{PL}$, $\triangle R_{WV}$, $\triangle R_{LR}$, $\triangle R_{CD}$, $\triangle R_{AL}$ represents the radiative energy flux anomaly ($W\,m^{-2}$) at the top of atmosphere (TOA) induced by the local deviation of Planck feedback (PL), water vapor feedback (WV), lapse-rate feedback (LR), cloud feedback (Cloud) and albedo feedback (Albedo), respectively. WV can be further decomposed into the longwave (LW_WV) and shortwave (SW_WV) components. Q_s is the surface heat source (SHEAT; $W\,m^{-2}$), $\triangle AET$ is the change in atmospheric horizontal energy transport (AHET; $W\,m^{-2}$). The calculation for each term is described in detail in Appendix A. All energy fluxes in Equation 1 are positive towards the atmosphere.

Figure 3a shows the result of the surface temperature change decomposition for the Sahara Desert and average tropical land. Note that in SSTONLY, the atmospheric forcings are turned off (F = 0) and are not shown in the figure. The residuals (Res) for the Sahara Desert (-0.03 K) and average tropical land (-0.04 K) are two and one orders of magnitude smaller than the corresponding modeled temperature change (Dts), indicating that the decomposition explains most of the Saharan and average tropical land warming (Figure 3a).

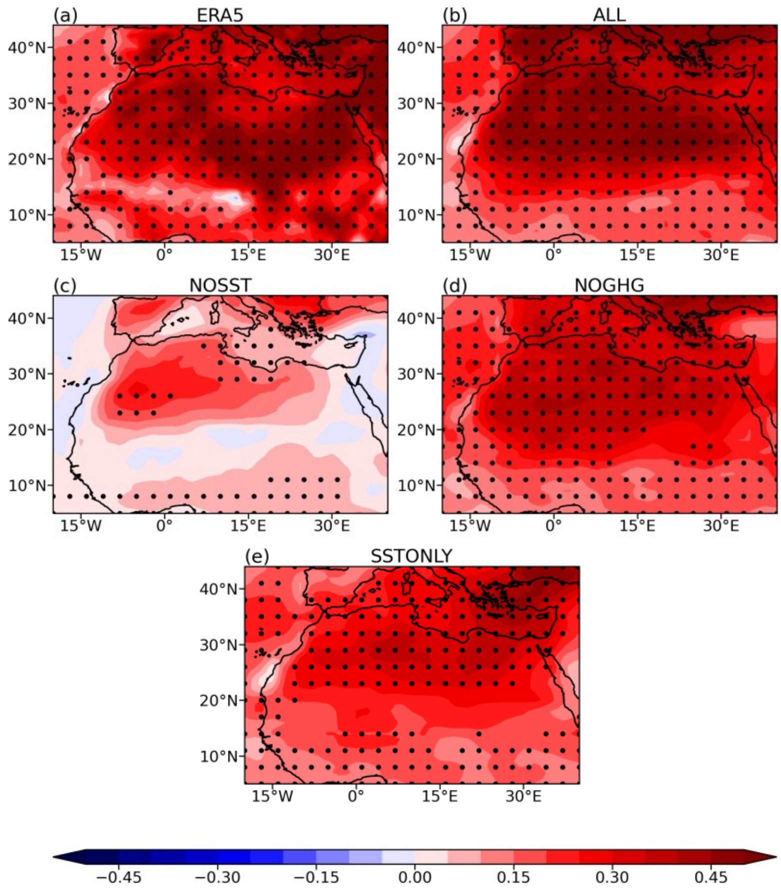

Figure 2. Spatial patterns of the SAT trends (K/decade) in the boreal warm season from (a) ERA5, (b) ALL, (c) NOSST, (d) NOGHG and (e) SSTONLY. The area dotted denotes the region with SAT trends that are statistically significant at the 99% level of confidence.

Figure 3a highlights the dominant role of the change in AHET (0.67 K) in the Saharan temperature increase. Change in AHET also dominates the temperature increase over the average tropical land (0.64 K). This indicates that as the ocean warms up, more energy is transported from the warming ocean to the land and warms the surface (Compo & Sardeshmukh (2009); Lambert et al. (2011); Toda et al. (2021)). It is interesting to note secondary contribution comes from the water vapor feedback, with the longwave and shortwave water vapor feedback in total explains about 0.58 K temperature increase (Figure 3a). This agrees well with previous work highlighting the strongest water vapor feedback over the driest regions on Earth (Vizy & Cook (2017); Zhou et al. (2016); Zhou (2016)). The dominant contributions of change in AHET and water vapor feedback suggests that without the anthropogenic GHG radiative forcing, AHET anomaly brought about by the warming ocean acts as the external forcing and increases the Saharan surface temperature (Lambert et al. (2011)). In the meantime, the temperature increase driven by the AHET anomaly is strongly amplified by the local water vapor feedback (Figure 3a).

It is noteworthy that the lapse-rate feedback favors the Saharan warming while hampering the temperature increase over the average tropical land (Figure 3a). The difference in lapse-rate feedback makes the largest contribution to the warming contrast between the Sahara Desert and average tropical land (Figure 3b). The discrepancy in lapse-rate feedback can be attributed to the different vertical warming profile between the average tropical land

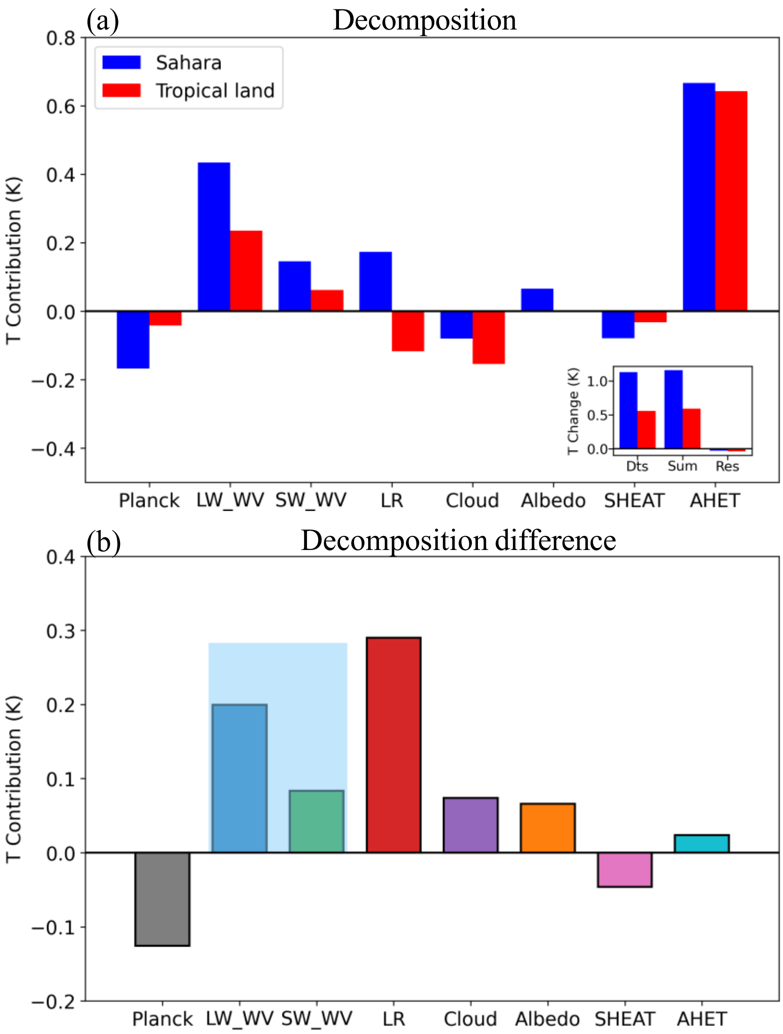

Figure 3. (a) Decomposition of the surface temperature change in boreal warm season for the Sahara Desert (blue) and average tropical land (red) in SSTONLY. Small figure inserted shows the left term (Dts), sum of the right terms (Sum), and the residual (Res) of Equation 1. (b) The difference for each term in (a) between Sahara Desert and the average tropical land. The transparent light blue bar denotes the total water vapor feedback difference (LW WV+SW_WV). Positive values denote that the term favors DA.

and Sahara Desert (Figure 4a). In SSTONLY, the average tropical land is characterized by a top-heavy warming profile, which dampens the surface warming (Figure 4a; Colman & Soden (2021); Soden et al. (2008)). In contrast to the average tropical land, Sahara Desert is characterized by a bottom-heavy warming profile, with the maximum temperature increase in the lower troposphere (Figure 4a). As a result, the lapse-rate feedback over the Sahara Desert acts to enhance the local temperature increase (Figure 3a). The unique bottom-heavy warming profile over the Sahara Desert has also been reported by previous studies based on observational (Wei et al. (2017)) and reanalysis datasets (Cook & Vizy (2015)). The Saharan bottom-heavy warming profile has also been found in ERA5 (Figure S1a). It is tempting to explain the top-heavy warming profile over the average tropical land in SSTONLY as a result of radiative-convective adjustment (Emanuel (2007); Holloway & Neelin (2007); Jeevanjee et al. (2022)). However, a recent result from Wang & Huang

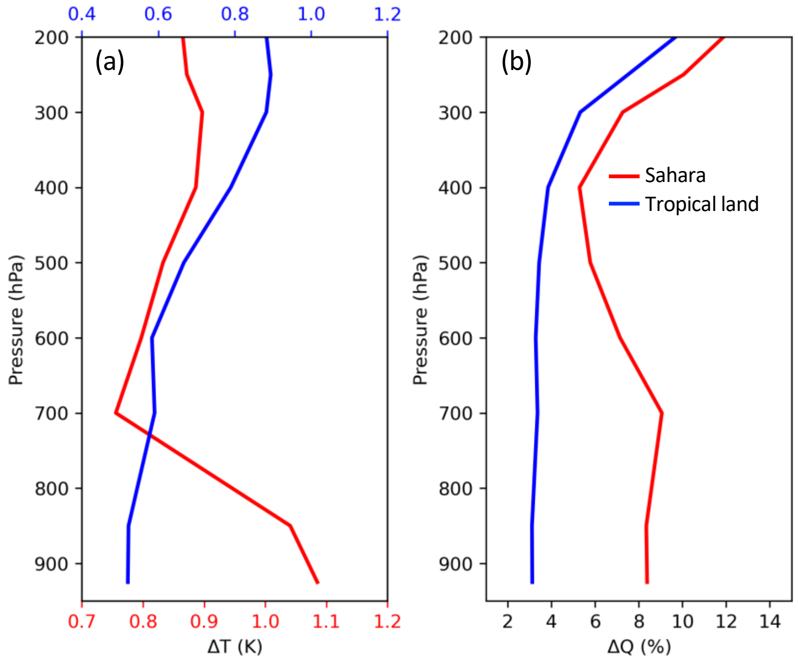

Figure 4. (a) Temperature change (K) in boreal warm season averaged over the Sahara Desert (red), tropical land (blue) as a function of pressure in SSTONLY. Saharan and tropical land temperature change corresponds to the bottom and top axis, respectively. (b) same as (a) but for the fractional change (%) in specific humidity (kg/kg).

(2021) shows that the circulation adjustment also plays an important role in shaping the lapse rate change over the tropics in response to SST increase. Previous work has also reported larger deviation of the tropical land from moist adiabatic than the tropical ocean (Byrne & O'Gorman (2013); Chiang & Lintner (2005); Jakob et al. (2019)), suggesting that the lapse rate change over the land in the tropics is more sensitive to processes other than radiative-convective adjustment relative to the tropical ocean. For this reason, we refrain from explaining the lapse-rate change over the average tropical land in SSTONLY from the moist adiabatic perspective solely. The relative contributions of radiation, convection and circulation adjustment to the change in the lapse rate over the Sahara Desert and average tropical land in response to the oceanic forcing needs further in-depth research in the future.

Apart from the lapse-rate feedback, water vapor feedback also favors DA (Figure 3b). The contribution of longwave and shortwave water vapor feedback in total to the warming contrast between Sahara Desert and the average tropical land is close to that of lapse-rate feedback (Figure 3b). The stronger water vapor feedback over the Sahara Desert is likely a result of the stronger Saharan moistening in comparison to the average tropical land (Figure 4b), which has also been highlighted in previous studies (Wei et al., 2017). However, the difference in the radiative kernel over the Sahara Desert and the average tropical land could also factor into the water vapor feedback discrepancy (Previdi et al. (2021)). Decomposition of the water vapor feedback difference into the moistening, radiative kernel and their covariance is beyond the scope of this paper and will be a subject of future studies.

It is worth noting that the water vapor and lapse-rate feedback have same signs over the Sahara Desert (Figure 3a), contrary to the conventional view that they generally counteract each other in the climate system (Colman (2003); Dessler (2013); Ingram (2013); Sanderson et al. (2010); Soden & Held (2006); Zhang et al. (1994)). The cancellation between the water vapor and lapse-rate feedback is argued to be closely tied to the deep intense convection (Hansen et al. (1984)); Taylor et al. (2011)). Our results hightlight that over extreme dry regions like the Sahara Desert in the tropics, lapse-rate and water vapor feedbacks are likely to both enhance the surface warming. It is worthwhile to check whether the same result applies to other dry regions on Earth, like the desert in Australia and the Arabian Peninsula in future studies.

Our result indicates that the lapse-rate change plays a predominant role in DA, which is broadly consistent with previous studies on land-ocean warming contrast (Byrne & O'Gorman (2013); Byrne & O'Gorman (2018); Joshi et al. (2008)) and Mediterranean amplification (Brogli et al. (2019); Kröner et al. (2017)). However, there is a lack of agreement on the role of water vapor feedback in land-sea warming contrast (Byrne & O'Gorman (2013); Dommenget & Flöter (2011); Toda et al. (2021)). Different from the results based on idealized simulations (Byrne & O'Gorman (2013)), Figures 3a and 3b indicate that water vapor feedback is an important contributor to the warming contrast between the Sahara Desert and average tropical land, alluding to the possibility that it could also factor into the difference between the Saharan and oceanic warming (Dommenget & Flöter (2011); Toda et al. (2021)). Our result also suggests the likelihood that water vapor feedback may make an important contribution to the land-sea warming contrast and Mediterranean amplification. Nevertheless, the prescription of SST in our study prevents us from assessing the effects of water vapor feedback on the warming contrast between Sahara Desert and the surrounding ocean. Simulations based on fully coupled ocean–atmosphere models are expected to be carried out in future studies to provide more insights into the role of water vapor feedback in the stronger warming of average tropical land, Sahara Desert and southern Europe than the ocean.

5 Conclusion and discussion

In this study, we quantify the relative contributions of the direct anthropogenic GHG radiative forcing and remote SST change to the observed Saharan warming in the boreal warm season since 1979 using AGCM simulations. The simulation forced with the observed monthly evolving SST, GHG and other atmospheric forcings reproduced the Saharan warming successfully in terms of the interannual variability and spatial warming pattern. The warming contrast between the Sahara Desert and the average tropical land is also well simulated in the experiment. By deactivating the anthropogenic GHG forcing and SST change separately in two mechanism-denial experiments, we found that the observed Saharan warming in the boreal warm season is predominantly determined by the remote SST forcing, which is consistent with previous work (Lambert & Chiang (2007); Skinner et al. (2012)). It is worthwhile to evaluate the contributions of SST change in different regions to the observed Saharan warming, which will help identify the ocean basin that predominates the Saharan temperature change. However, such examination needs additional experiments that deactivate the SST forcing in different ocean basins (Kosaka & Xie (2013); Park et al. (2016)), which is beyond the scope of this study and will be left to a future work.

The surface temperature decomposition technique based on the atmospheric energy budget is employed in this study to explore the mechanism responsible for the SST forcing-induced Saharan temperature increase. In the experiment with only the SST forcing on, the largest contribution to the Saharan temperature increase comes from the change in atmospheric horizontal energy transport. This is consistent with the conclusion of Lambert et al. (2011) that without the direct anthropogenic GHG forcing, the extra energy from the ocean acts as the external forcing and drives the land warming. The second largest term from the budget is the water vapor feedback, which is in line with previous work highlighting the strong water vapor feedback over the Sahara Desert (Zhou et al. (2016)). Our result indicates that change in energy transport plays a leading role in the observed Saharan warming. Examination of the change in sensible and latent energy flux into the Sahara Desert is not conducted in this paper and will be a subject of future study. Another interesting issue unexplored is the vertical structure of the change in energy flux into the Sahara Desert. Recent studies showed that the vertical structure of the energy flux into the Arctic has important implications for the Arctic amplification (Cardinale et al. (2021); Cardinale & Rose (2022); Cardinale & Rose (2023)). Exploration of the corresponding vertical structure over the Sahara Desert and the link to the Saharan warming also needs further in-depth research.

The feature of DA is also present in our simulations. As the SST forcing accounts for most of the Saharan warming, we focus on the warming contrast between the Sahara Desert and average tropical land under the same SST forcing. The result from the surface temperature decomposition highlights the central role of lapse-rate feedback in DA. The warming profile over the Sahara Desert features a bottom-heavy vertical structure, making the lapse-rate feedback positive and favoring Saharan warming, which is different from the average tropical land. Previous work argues that the water vapor feedback and lapse-rate feedback tend to have opposing signs in most regions (Held & Shell (2012); Lambert & Taylor (2014); Soden & Held (2006); Taylor et al. (2011)). Our result indicates that the Sahara Desert is the exception in that the water vapor feedback and lapse-rate feedback over this area both enhances the surface warming. The key question unexplored in our study is the physical process responsible for the bottom-heavy Saharan warming profile. Located in the descending branch of the Hadley cell, Sahara Desert is different from the average tropical land and far from radiative-convective equilibrium because the convective activity is strongly dampened in this area. Different physical processes may interact or compete with each other in determining the lapse-rate change over the Sahara Desert. Unraveling the underlying physical mechanism for the bottom-heavy warming profile over the Sahara Desert will also shed light on the consistency between the effects of the lapse-rate and water vapor feedback on the Saharan warming. Attribution of the lapse-rate change over the Sahara Desert into different physical process will be the subject of future studies. Another interesting feature from the temperature decomposition is the positive albedo feedback over the Sahara Desert (Figure 3a), which is likely a result of the change in soil moisture. As the Sahara Desert is projected to become more humid in the end of the 21st century (Pausata et al. (2020)), it may be worthwhile to evaluate the effects of albedo feedback on the Saharan warming in the 21st century in future studies.

Appendix A Calculation of each term in Equation 1

The radiative kernels and difference in the variables from two climate states are used to calculate the climate feedbacks in Equation 1 (Block & Mauritsen (2013); Jenkins & Dai (2021); Soden et al. (2008)):

$$\triangle R_{PL} = K_{ts} * \triangle T_s + \int_{p_0}^{p_{TOA}} K_{ta} * \triangle T_a \, dp, \tag{A1}$$

$$\triangle R_{WV} = \int_{p_0}^{p_{TOA}} K_w * \triangle q \, dp, \tag{A2}$$

$$\triangle R_{LR} = \int_{p_0}^{p_{TOA}} K_{ta} * (\triangle T_a - \triangle T_s) \, dp, \tag{A3}$$

$$\begin{aligned} \triangle R_{CD} = dC_{RF} - (K_a - K_a^c) * \triangle a - (K_{ts} - K_{ts}^c) * \triangle T_s - \int_{p_0}^{p_{TOA}} (K_{ta} - K_{ta}^c) * \triangle T_a \, dp \\ - \int_{p_0}^{p_{TOA}} (K_w - K_w^c) * \triangle q \, dp - (G - G^c), \end{aligned} \tag{A4}$$

$$\triangle R_{AL} = K_a * \triangle a, \tag{A5}$$

where K_{ts}, K_{ta}, K_w, K_a denotes the all-sky surface temperature, atmospheric temperature, water vapor and albedo kernel at TOA, respectively. $\triangle$ represents the difference between two climate states. T_a and q are the temperature (K) and specific humidity ($kg\ kg^{-1}$) on the every pressure level. a is the surface albedo. p_0 and p_{TOA} are the pressure at the surface and tropopause, respectively. p_{TOA} is prescribed as 100 hPa at the Equator and decreases by cosine of latitude to 300 hPa at Poles (Pendergrass et al. (2018)). dC_{RF} represents the cloud radiative effect, which is estimated as the change in the cloud radiative forcing between two climate states (Soden et al. (2008)). K^c_{ts}, K^c_{ta}, K^c_w, K^c_a are the corresponding clear-sky kernels. G and G^c are the all-sky and clear-sky forcing from GHG or aerosols. Note that in SSTONLY, both G and G^c equal to zero as the GHG and aerosol forcing are turned off.

The surface heat source (Q_s) is estimated as the change in the surface energy flux (R_{BOA}) from two climate states. The surface energy flux includes the surface sensible heat flux, latent heat flux and net radiation flux. $\triangle AET$ is estimated based on the difference between the surface heat source, TOA energy flux (R_{TOA}) and atmospheric energy storage change ($\frac{\partial E}{\partial t}$):

$$\triangle AET = \triangle(R_{BOA} - R_{TOA} + \frac{\partial E}{\partial t}), \tag{A6}$$

where E is the vertically integrated moist static energy from the surface to tropopause. According to our calculation, the atmospheric energy storage change is two orders of magnitude smaller than the change in energy flux in Equation A6.

Appendix B Open Research

The model simulation data are available in Zhuo (2023).

Acknowledgments

This research is supported by the National Science Foundation (NSF) (AGS-1952745). The first author thanks Matthew Jenkins for the insightful discussions on the climate feedback calculation using radiative kernels. Gratitude is extended to two anonymous reviewers for the insightful comments and suggestions that helped improve the quality of our work.

References

Andrews, T., Forster, P. M., & Gregory, J. M. (2009). A surface energy perspective on climate change. *Journal of Climate*, *22*(10), 2557–2570.

Block, K., & Mauritsen, T. (2013). Forcing and feedback in the mpi-esm-lr coupled model under abruptly quadrupled co2. *Journal of Advances in Modeling Earth Systems*, *5*(4), 676–691.

Brogli, R., Kröner, N., Sørland, S. L., Lüthi, D., & Schär, C. (2019). The role of hadley circulation and lapse-rate changes for the future european summer climate. *Journal of Climate*, *32*(2), 385–404.

Byrne, M. P. (2021). Amplified warming of extreme temperatures over tropical land. *Nature Geoscience*, *14*(11), 837–841.

Byrne, M. P., & O'Gorman, P. A. (2013). Land–ocean warming contrast over a wide range of climates: Convective quasi-equilibrium theory and idealized simulations. *Journal of Climate*, *26*(12), 4000–4016.

Byrne, M. P., & O'Gorman, P. A. (2018). Trends in continental temperature and humidity directly linked to ocean warming. *Proceedings of the National Academy of Sciences*, *115*(19), 4863–4868.

Cardinale, C. J., & Rose, B. E. (2022). The arctic surface heating efficiency of tropospheric energy flux events. *Journal of Climate*, *35*(18), 5897–5913.

Cardinale, C. J., & Rose, B. E. (2023). The increasing efficiency of the poleward energy transport into the arctic in a warming climate. *Geophysical Research Letters*, *50*(2), e2022GL100834.

Cardinale, C. J., Rose, B. E., Lang, A. L., & Donohoe, A. (2021). Stratospheric and tropospheric flux contributions to the polar cap energy budgets. *Journal of Climate*, *34*(11), 4261–4278.

Chiang, J. C., & Lintner, B. R. (2005). Mechanisms of remote tropical surface warming during el niño. *Journal of climate*, *18*(20), 4130–4149.

Colman, R. (2003). A comparison of climate feedbacks in general circulation models. *Climate Dynamics*, *20*(7-8), 865–873.

Colman, R., & Soden, B. J. (2021). Water vapor and lapse rate feedbacks in the climate system. *Reviews of Modern Physics*, *93*(4), 045002.

Compo, G. P., & Sardeshmukh, P. D. (2009). Oceanic influences on recent continental warming. *Climate Dynamics*, *32*, 333–342.

Cook, K. H., & Vizy, E. K. (2015). Detection and analysis of an amplified warming of the sahara desert. *Journal of Climate*, *28*(16), 6560–6580.

Deser, C., Alexander, M. A., Xie, S.-P., & Phillips, A. S. (2010). Sea surface temperature variability: Patterns and mechanisms. *Annual review of marine science*, *2*, 115–143.

Deser, C., & Phillips, A. S. (2009). Atmospheric circulation trends, 1950–2000: The relative roles of sea surface temperature forcing and direct atmospheric radiative forcing. *Journal of Climate*, *22*(2), 396–413.

Dessler, A. E. (2013). Observations of climate feedbacks over 2000–10 and comparisons to climate models. *Journal of Climate*, *26*(1), 333–342.

Dommenget, D. (2009). The ocean's role in continental climate variability and change. *Journal of Climate*, *22*(18), 4939–4952.

Dommenget, D., & Flöter, J. (2011). Conceptual understanding of climate change with a globally resolved energy balance model. *Climate dynamics*, *37*, 2143–2165.

Emanuel, K. (2007). Quasi-equilibrium dynamics of the tropical atmosphere. *The Global Circulation of the Atmosphere*, *186*, 218.

Evan, A. T., Flamant, C., Lavaysse, C., Kocha, C., & Saci, A. (2015). Water vapor–forced greenhouse warming over the sahara desert and the recent recovery from the sahelian drought. *Journal of Climate*, *28*(1), 108–123.

Folland, C. K., Sexton, D. M., Karoly, D. J., Johnson, C. E., Rowell, D. P., & Parker, D. E. (1998). Influences of anthropogenic and oceanic forcing on recent climate change. *Geophysical Research Letters*, *25*(3), 353–356.

Gent, P. R., Danabasoglu, G., Donner, L. J., Holland, M. M., Hunke, E. C., Jayne, S. R., ... others (2011). The community climate system model version 4. *Journal of climate*, *24*(19), 4973–4991.

Goosse, H., Kay, J. E., Armour, K. C., Bodas-Salcedo, A., Chepfer, H., Docquier, D., ... others (2018). Quantifying climate feedbacks in polar regions. *Nature communications*, *9*(1), 1919.

Hansen, J., Lacis, A., Rind, D., Russell, G., Stone, P., Fung, I., ... Lerner, J. (1984). Climate sensitivity: Analysis of feedback mechanisms. *Climate processes and climate sensitivity*, *29*, 130–163.

He, J., & Soden, B. J. (2015). Anthropogenic weakening of the tropical circulation: The relative roles of direct co2 forcing and sea surface temperature change. *Journal of Climate*, *28*(22), 8728–8742.

Held, I. M., & Shell, K. M. (2012). Using relative humidity as a state variable in climate feedback analysis. *Journal of Climate*, *25*(8), 2578–2582.

Henry, M., Merlis, T. M., Lutsko, N. J., & Rose, B. E. (2021). Decomposing the drivers of polar amplification with a single-column model. *Journal of Climate*, *34*(6), 2355–2365.

Hersbach, H., Bell, B., Berrisford, P., Hirahara, S., Horányi, A., Muñoz-Sabater, J., ... others (2020). The era5 global reanalysis. *Quarterly Journal of the Royal Meteorological Society*, *146*(730), 1999–2049.

Holloway, C. E., & Neelin, J. D. (2007). The convective cold top and quasi equilibrium. *Journal of the atmospheric sciences*, *64*(5), 1467–1487.

Hurrell, J. W., Hack, J. J., Shea, D., Caron, J. M., & Rosinski, J. (2008). A new sea surface temperature and sea ice boundary dataset for the community atmosphere model. *Journal of Climate*, *21*(19), 5145–5153.

Hurrell, J. W., Holland, M. M., Gent, P. R., Ghan, S., Kay, J. E., Kushner, P. J., ... others (2013). The community earth system model: a framework for collaborative research. *Bulletin of the American Meteorological Society*, *94*(9), 1339–1360.

Ingram, W. (2013). Some implications of a new approach to the water vapour feedback. *Climate Dynamics*, *40*(3-4), 925–933.

Jakob, C., Singh, M., & Jungandreas, L. (2019). Radiative convective equilibrium and organized convection: An observational perspective. *Journal of Geophysical Research: Atmospheres*, *124*(10), 5418–5430.

Jeevanjee, N., Held, I., & Ramaswamy, V. (2022). Manabe's radiative–convective equilibrium. *Bulletin of the American Meteorological Society*, *103*(11), E2559–E2569.

Jenkins, M., & Dai, A. (2021). The impact of sea-ice loss on arctic climate feedbacks and their role for arctic amplification. *Geophysical Research Letters*, *48*(15), e2021GL094599.

Joshi, M. M., Gregory, J. M., Webb, M. J., Sexton, D. M., & Johns, T. C. (2008). Mechanisms for the land/sea warming contrast exhibited by simulations of climate change. *Climate dynamics*, *30*, 455–465.

Kosaka, Y., & Xie, S.-P. (2013). Recent global-warming hiatus tied to equatorial pacific surface cooling. *Nature*, *501*(7467), 403–407.

Kröner, N., Kotlarski, S., Fischer, E., Lüthi, D., Zubler, E., & Schär, C. (2017). Separating climate change signals into thermodynamic, lapse-rate and circulation effects: theory and application to the european summer climate. *Climate Dynamics*, *48*, 3425–3440.

Lambert, F. H., & Chiang, J. C. (2007). Control of land-ocean temperature contrast by ocean heat uptake. *Geophysical research letters*, *34*(13).

Lambert, F. H., & Taylor, P. C. (2014). Regional variation of the tropical water vapor and lapse rate feedbacks. *Geophysical Research Letters*, *41*(21), 7634–7641.

Lambert, F. H., Webb, M. J., & Joshi, M. M. (2011). The relationship between land–ocean surface temperature contrast and radiative forcing. *Journal of Climate*, *24*(13), 3239–3256.

Lavaysse, C., Flamant, C., Evan, A., Janicot, S., & Gaetani, M. (2016). Recent climatological trend of the saharan heat low and its impact on the west african climate. *Climate Dynamics*, *47*, 3479–3498.

Li, X., Ting, M., You, Y., Lee, D.-E., Westervelt, D. M., & Ming, Y. (2020). South asian summer monsoon response to aerosol-forced sea surface temperatures. *Geophysical Research Letters*, *47*(1), e2019GL085329.

Liu, P., Meehl, G. A., & Wu, G. (2002). Multi-model trends in the sahara induced by increasing co2. *Geophysical Research Letters*, *29*(18), 28–1.

Liu, P., Washington, W. M., Meehl, G. A., Wu, G., & Potter, G. L. (2001). Historical and future trends of the sahara desert. *Geophysical research letters*, *28*(14), 2683–2686.

Park, J.-y., Bader, J., & Matei, D. (2016). Anthropogenic mediterranean warming essential driver for present and future sahel rainfall. *Nature Climate Change*, *6*(10), 941–945.

Pausata, F. S., Gaetani, M., Messori, G., Berg, A., de Souza, D. M., Sage, R. F., & De-Menocal, P. B. (2020). The greening of the sahara: Past changes and future implications. *One Earth*, *2*(3), 235–250.

Pendergrass, A. G., Conley, A., & Vitt, F. M. (2018). Surface and top-of-atmosphere radiative feedback kernels for cesm-cam5. *Earth System Science Data*, *10*(1), 317–324.

Pithan, F., & Mauritsen, T. (2014). Arctic amplification dominated by temperature feedbacks in contemporary climate models. *Nature geoscience*, *7*(3), 181–184.

Previdi, M., Smith, K. L., & Polvani, L. M. (2021). Arctic amplification of climate change: a review of underlying mechanisms. *Environmental Research Letters*, *16*(9), 093003.

Sanderson, B. M., Shell, K. M., & Ingram, W. (2010). Climate feedbacks determined using radiative kernels in a multi-thousand member ensemble of aogcms. *Climate dynamics*, *35*, 1219–1236.

Shaw, T., & Voigt, A. (2015). Tug of war on summertime circulation between radiative forcing and sea surface warming. *Nature Geoscience*, *8*(7), 560–566.

Shen, Z., Ming, Y., & Held, I. M. (2020). Using the fast impact of anthropogenic aerosols on regional land temperature to constrain aerosol forcing. *Science Advances*, *6*(32), eabb5297.

Skinner, C. B., Ashfaq, M., & Diffenbaugh, N. S. (2012). Influence of twenty-first-century atmospheric and sea surface temperature forcing on west african climate. *Journal of Climate*, *25*(2), 527–542.

Soden, B. J., & Held, I. M. (2006). An assessment of climate feedbacks in coupled ocean–atmosphere models. *Journal of climate*, *19*(14), 3354–3360.

Soden, B. J., Held, I. M., Colman, R., Shell, K. M., Kiehl, J. T., & Shields, C. A. (2008). Quantifying climate feedbacks using radiative kernels. *Journal of Climate*, *21*(14), 3504–3520.

Stuecker, M. F., Bitz, C. M., Armour, K. C., Proistosescu, C., Kang, S. M., Xie, S.-P., . . . others (2018). Polar amplification dominated by local forcing and feedbacks. *Nature Climate Change*, *8*(12), 1076–1081.

Taylor, P. C., Ellingson, R. G., & Cai, M. (2011). Geographical distribution of climate feedbacks in the ncar ccsm3. 0. *Journal of climate*, *24*(11), 2737–2753.

Toda, M., Watanabe, M., & Yoshimori, M. (2021). An energy budget framework to understand mechanisms of land–ocean warming contrast induced by increasing greenhouse gases. part i: Near-equilibrium state. *Journal of Climate*, *34*(23), 9279–9292.

Trenberth, K. E., Smith, L., Qian, T., Dai, A., & Fasullo, J. (2007). Estimates of the global water budget and its annual cycle using observational and model data. *Journal of Hydrometeorology*, *8*(4), 758–769.

Vizy, E. K., & Cook, K. H. (2017). Seasonality of the observed amplified sahara warming trend and implications for sahel rainfall. *Journal of Climate*, *30*(9), 3073–3094.

Wang, Y., & Huang, Y. (2021). A single-column simulation-based decomposition of the tropical upper-tropospheric warming. *Journal of Climate*, *34*(13), 5337–5348.

Wei, N., Zhou, L., Dai, Y., Xia, G., & Hua, W. (2017). Observational evidence for desert amplification using multiple satellite datasets. *Scientific Reports*, *7*(1), 2043.

Zhang, M., Hack, J., Kiehl, J., & Cess, R. (1994). Diagnostic study of climate feedback processes in atmospheric general circulation models. *Journal of Geophysical Research: Atmospheres*, *99*(D3), 5525–5537.

Zhou, L. (2016). Desert amplification in a warming climate. *Scientific Reports*, *6*(1), 31065.

Zhou, L. (2021). Diurnal asymmetry of desert amplification and its possible connections to planetary boundary layer height: a case study for the arabian peninsula. *Climate Dynamics*, *56*(9-10), 3131–3156.

Zhou, L., Chen, H., & Dai, Y. (2015). Stronger warming amplification over drier ecoregions observed since 1979. *Environmental Research Letters*, *10*(6), 064012.

Zhou, L., Chen, H., Hua, W., Dai, Y., & Wei, N. (2016). Mechanisms for stronger warming over drier ecoregions observed since 1979. *Climate dynamics*, *47*, 2955–2974.

Zhuo, L. (2023). *Model simulations* [Dataset]. Zenodo. Retrieved from https://zenodo.org/records/10019700

Zhuo, L., & Zhou, L. (2022). Moisture transport and water vapour budget over the sahara desert. *International Journal of Climatology*, *42*(13), 6829–6843.